Large format MBE HgCdTe on silicon detector development for astronomy

Brandon J. Hanold[a], Donald F. Figer[a], Joong Lee[a], Kimberly Kolb[a], Iain Marcuson[a], Elizabeth Corrales[b], Jonathan Getty[b], Lynn Mears[b]
[a]Rochester Institute of Technology, 74 Lomb Memorial Dr., Rochester, NY, 14623; [b]Raytheon Vision Systems, 75 Coromar Dr., Goleta, CA 93117

ABSTRACT

The Center for Detectors at Rochester Institute of Technology and Raytheon Vision Systems (RVS) are leveraging RVS capabilities to produce large format, short-wave infrared HgCdTe focal plane arrays on silicon (Si) substrate wafers. Molecular beam epitaxial (MBE) grown HgCdTe on Si can reduce detector fabrication costs dramatically, while keeping performance competitive with HgCdTe grown on CdZnTe. Reduction in detector costs will alleviate a dominant expense for observational astrophysics telescopes. This paper presents the characterization of 2.5µm cutoff MBE HgCdTe/Si detectors including pre- and post-thinning performance. Detector characteristics presented include dark current, read noise, spectral response, persistence, linearity, crosstalk probability, and analysis of material defects.

Keywords: HgCdTe, HgCdTe on Si, MCT,MBE, VIRGO, SWIR, FPA, Detector

1. INTRODUCTION

Infrared HgCdTe (MCT) detector(s) grown on Si cost less than using CdZnTe (CZT) (Bangs, et al., 2011). Larger wafer size allows for larger die and more die per wafer which in turn reduces cost. The Center for Detectors (CfD) at the Rochester Institute of Technology (RIT) and Raytheon Vision Systems (RVS) are developing infrared detectors for astronomy with the use of Si substrate wafers. The goal of the current effort is to produce a 2K×2K MBE MCT/Si detector with competitive performance, and the longer-term goal is to produce an 8K×8K version of this device (Table 1).

Today, a typical state-of-the-art 2K×2K or 4K×4K device can cost a significant fraction of the total cost of an astronomical instrument. Infrared detectors are expensive, and this is the primary constraint that prevents their use in greater numbers. Small telescopes (D~1 m) rarely have infrared instruments, and even moderately-sized telescopes (D~3 m) often have only one infrared instrument that is usually an imager. While large telescopes (D~8-10 m) now typically have multiple infrared instruments, their focal planes are sparsely populated, again often due to the cost of infrared detectors. The infrared discovery space for all of these facilities is primarily constrained by the cost of large format infrared detectors.

Past experiences have shown that investment in detector technology results in high return for astronomy. In today's tight budget environment, technologies that can reduce detector development cost and increase large format detector array yield will be critical to making future observatories more affordable and leverage investments in existing observatories. The astronomy community will commit a significant amount of money to detectors in the next 10 years, and affordable large-format infrared detectors will be crucial. (Svitak, 2013)

Si wafers are the primary material for semiconductor circuit substrates and are thus pervasive in the semiconductor industry. Given their daily use in very high volume, and general availability, they are inexpensive, on the order of zero cost in the context of scientific detectors. They are also readily available in large sizes. This is unlike substrates of more exotic materials, e.g., CZT, which have very limited commercial use, are produced in low volumes, are available through a small set of vendors, and come in very small sizes. Commonly-available Si wafers have sizes of 8-12 inches (and increasing) which would accommodate 8K×8K (64 Mpixel) or 14K×14K (200 Mpixel) arrays with 15 µm pixels.

This development has ancillary benefits for NASA Astrophysics, Earth Science, and Planetary Science missions. Note that large format VIS/IR detectors are one of four key enabling technologies for future Earth Science space missions for characterization of weather, climate, and air pollution, as described by Puschell (2009).

The chosen technology of MCT on Si provides high sensitivity, broad wavelength coverage from the optical to infrared, low noise, low dark current, low inter-pixel capacitance (IPC), low cost, and scalability to very large format sizes. By maturing this material and processing system, astronomers will have powerful new tools for fabricating extremely large infrared focal planes. The plan includes design and fabrication of test structures and hybridized focal planes in 1K×1K and 2K×2K pixel formats.

In Phase I of the project, CfD and RVS designed, fabricated, and tested new infrared detectors based on HgCdTe (MCT) light-sensing material deposited on Si wafers. The effort validated key principles of the technology and demonstrated that it will be successful for astronomy. The history leading up to this development is reviewed in Melkonian et al. (2010), Bangs et al. (2011), Reddy et al. (2011), and Gulbransen et al. (2004). This effort will not only provide cost savings, but it will also provide 1K, 2K and 4K detectors in a single run. MCT/Si has been in full rate production for several years at RVS for tactical "high background" applications. The parts fabricated in phase I do not satisfy all the goals due to contamination in the first fabrication run. However, the parts were tested to learn how to modify the design of the second run to be within reach of the goals.

The performance goals of Phase I are shown in Table 1. The delivered performance is in the column on the right. In general, the devices satisfy the proposed performance, except in dark current. Some of the devices have a significant dark current tail that skews the median of the distribution to higher values and effectively reduces the fraction of pixels that satisfy the dark current requirement to ~70%, as compared to the required 98%.

Table 1. Phase I Goals and Progress. The table summarizes the goals of the funded project to develop MCT on Si and the current detector performance for comparison.

Parameter	SATIN Goal	Achieved
Format	1K×1K, 2K×2K	1K×1K, 2K×2K
Pixel Size	20 µm	20 µm
Read Noise (Fowler-16)	5 e−	6 e−
Wavelength Range	0.4 – 2.5 µm	0.5 – 2.5 µm
Dark Current (e–/s/pixel)	<0.05 @ 80 (98% Operability)	<0.05 @ 80 (70% Operability)
Well size (e–)	300,000	400,000
DQE (w/AR coating)	>70%	>75%
Persistence	<0.1%	<0.1%
Substrate	Si	Si
Number of readouts	4, 16	4, 16
Reference pixels	Yes	Yes
Reference outputs	Yes	No

2. DETECTOR DESIGN

In semiconductor growth, it is desirable to grow epitaxial layers with the same lattice constant (inter-atomic spacing) as the substrate material, with the substrate having a large enough energy gap for infrared transmission. HgCdTe is typically grown on CdZnTe, with 1-2% Zn added to reduce the lattice constant of CdTe (which slightly exceeds that of HgCdTe). As shown in Figure 1, there is no large-area substrate that matches HgCdTe's lattice constant (a). When grown on Si (which has a 19% smaller lattice constant), HgCdTe's lattice does not match up, leading to missing chemical bonds (b).

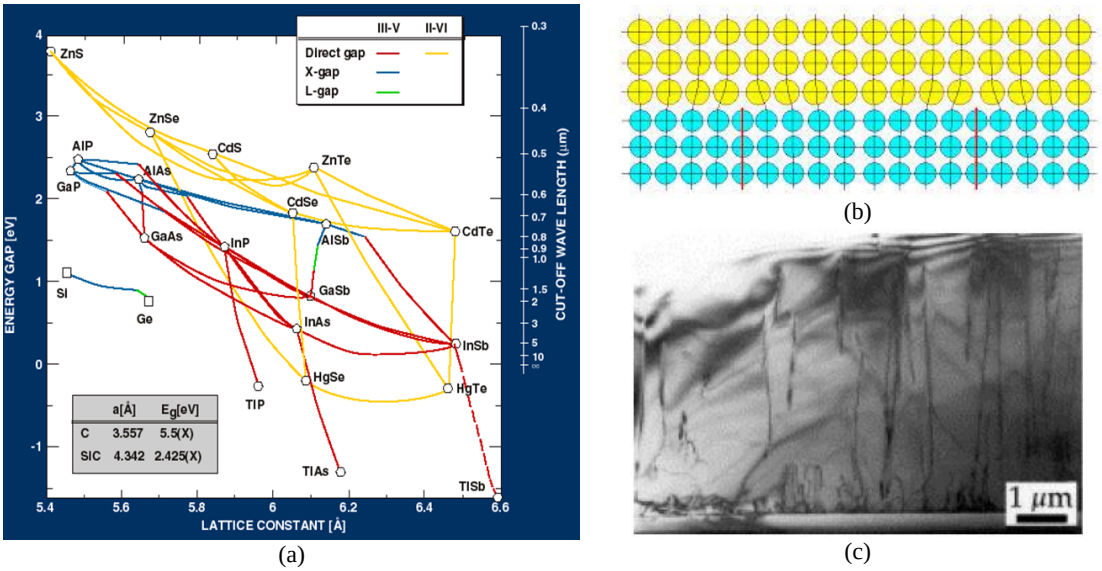

(a) (b) (c)

Figure 1. The lattice spacing for HgCdTe, CdZnTe, and CdTe are similar to within a few percent, but very different than the spacing for Si (a). The lattice mismatch leads to dislocations (b) which make threading dislocations that grow into the device (c).The figures are from Jóźwikowski, et. al. (2012)

Each of these missing bonds creates a defect that can grow upward (c) into the HgCdTe absorber if uncorrected (Jóźwikowski, Jóźwikowska, Kopytko, Rogalski, & Jaroszewicz, 2012). Where dislocations intersect the depletion region, there is an increase in dark current; where multiple dislocations overlap, an exponential increase in dark current is observed. Thus, it is essential that dislocation densities are low enough (typically 10^5-10^6 cm^{-2}) to prevent significant coupling between dislocations.

Defects are reduced by growing epitaxial buffer layers (Figure 2) that terminate the growth of the defects before they reach the detective layers and pn-junction. During the first attempts at growing short-wavelength HgCdTe on Si (in 2003, alongside the VISTA telescope detector effort), a thick buffer design was used. This reduced the dislocation density in the absorber layer, but the buffer layers used at that time absorbed wavelengths shorter than 1.6 μm, and caused significant mechanical stresses when cooled, often cracking the detector at cryogenic temperatures. To address these issues, a thinner buffer design was developed using wider-bandgap materials. This eliminates cracking and short-wavelength absorption, while providing low defect density.

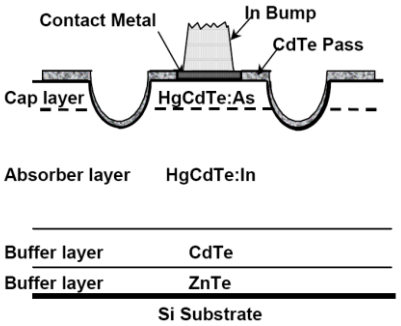

Figure 2. Buffer layers mediate the lattice spacing mismatch.

Development Summary

RIT has received a total of ten devices including the two benchmark devices (Table 2). The two benchmark devices were fabricated prior to this project (titled SATIN), they were provided to RIT for characterization. The results gave a benchmark to compare the SATIN devices against. VIRGO-9A is a MCT/CZT device and VIRGO-14 is a MCT/Si device. Having one device from each substrate material gave a comprehensive data set to compare the SATIN devices against. Eight additional devices have been tested from 4 wafers across two fabrication runs. Not all tests have been done for every part as seen in Table 2. Rather, specific tests were selected for certain parts in order to diagnose changes in the design and fabrication recipes. In this text, the detectors will be referred to by their identifier (i.e. VIRGO-F3 will be called F3).

Six of the devices tested were the variable unit cell (VUC) devices, denoted with a “V” in their identifier. Because smaller mesas are likely to have lower absolute dark current, but (beyond a critical trench width) lower quantum efficiency, several die on each wafer were printed with variable nominal mesa sizes of 13, 15, 17, and 18 μm mesas.

Dark current and quantum efficiency varied as expected, but due to low hole carrier lifetime, the best trade of response and dark current corresponded to a 17 µm mesa. This suggests that lateral collection was limited to <2 µm, which significantly limits crosstalk by photo-holes in the n-type absorber. Photo-electrons in the p-type cap are longer-lived, but are confined to the mesa top. Results from the VUC devices gave feedback to the fabrication process which corrected observed issues. All devices for this project have a 20 µm pixel pitch.

Table 2 This table shows the devices that were delivered for this project along with a list of performance metrics that were measured. The top two are heritage devices for benchmark testing. The "V" devices have a four variable unit cell (VUC) designs. The "F" devices were designed and fabricated from a second fabrication run after testing the VUC devices.

Detector	Format	Cutt-off (µm)	Substrate	Dark Current	Egain	Photon Transfer	Read Noise	Full Well	Linearity	Quantum Efficiency	Crosstalk	Persistence	Intra-pixel Sensitivity
VIRGO-9A	2K×2K	1.7	CZT	✓	✓	✓	✓	✓	✓	✓	✓	✓	✓
VIRGO-14	2K×2K	2.5	Si	✓	✓	✓	✓	✓	✓	✓	✓	✓	
VIRGO-V1	1K×1K	2.5	Si	✓	✓	✓				✓			
VIRGO-V2	1K×1K	2.5	Si	✓	✓	✓				✓			
VIRGO-V4	1K×1K	2.5	Si	✓	✓	✓				✓			
VIRGO-V5	1K×1K	2.5	Si	✓	✓	✓				✓			
VIRGO-V6	1K×1K	2.5	Si	✓	✓	✓				✓			
VIRGO-F3	1K×1K	2.5	Si	✓	✓	✓	✓	✓	✓	✓	✓	✓	
VIRGO-F6	1K×1K	2.5	Si	✓	✓	✓	✓	✓	✓	✓	✓	✓	
VIRGO-VTHIN1	1K×1K	2.5	Si	✓	✓	✓		✓	✓	✓	✓	✓	

Figure 3 (a) shows an example of MBE-grown HgCdTe on Si substrate wafer fabricated for the SATIN project. They have a p-type cap layer atop an n-type absorber layer. Underneath, buffer layers allow a lower-dislocation growth despite the significant lattice mismatch of HgCdTe and Si. Trenches are etched through the pn-junction, isolating each pixel's p-region and pn-junction from its neighbors. The mesas are passivated with CdTe and overglass. After dicing, the arrays are hybridized to readout integrated circuits via indium bumps located in each unit. The cross-section structure is shown in Figure 2.

Figure 3 (b) is an image from a VUC device showing the quad structure. The device is divided into quadrants as noted. The mesa size (µm) for each quadrant is noted in the corners. The device characteristics were tested in each quadrant and compared to determine the optimal pixel design. The quadrant structure within the four quadrants is due to stitching effects in the device fabrication. This was corrected in a second fabrication run.

(a) (b)

Figure 3. (a) The image shows a wafer that has 2K and 1K die, including 1K versions that have VUC designs. (b) The picture shows a dark image taken with one of the VUC devices with the mesa size (µm)..

The second fabrication run was completed using a tuned process based on the analysis of the VUC devices from the initial fabrication run to optimize the carrier lifetime with the 17 µm mesa. F3, F6, and VTHIN1 were packaged and characterized from the second fabrication run; this paper focuses on results from these devices. The results from the first fabrication run, VUC devices, are reported in Hanold, et al. (2013). An additional component of this development is device thinning to achieve both visible and infrared sensitivity. Post thinning results were measured on VTHIN1 which, came from the same wafer as F6. The thinned results are compared to F6 to analyze the thinning process and its impact on device performance.

3. DETECTOR CHARACTERIZAION

Characterization was done in the Rochester Imaging Detector Laboratory (RIDL), within the CfD. Shown in Figure 4 is one of the systems used to characterize the detectors. The system consists of software and hardware that has been used extensively to characterize infrared and optical detectors for space- and ground-based applications (Figer, et al., 2002), (Figer, et al., 2003), (Simms, et al., 2007).

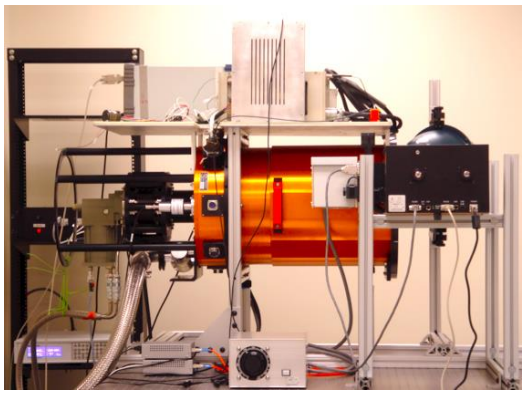

Figure 4. Pictured is a RIDL system. An orange dewar houses two filter wheels and a detector enclosure. A helium cryo-cooler cools the system. An integrating sphere and monochromator near the front of the dewar supplies monochromatic flat field illumination.

The modular architecture of the system allows for rapid acquisition and reduction of large datasets over a broad range of experimental conditions. Minimal effort is required to change between different detectors and different types of detectors. The system in Figure 4 can be transported for operation on a telescope or a radiation beam. The system includes a 40 cm diameter dewar (Universal Cryogenics, Tucson, AZ) with a 110 mm diameter CaF_2 window, two cryogenic filter wheels, and a detector enclosure. The system is cooled with a two-stage cooler (CTI Model 1050, Brooks Automation, Chelmsford, MA), and the detector is thermally stabilized with a 10-channel temperature controller (Lakeshore Cryotronics, Westerville, OH). The detector enclosure provides thermal and electrical feedthroughs, an entrance window, and an otherwise light-tight cavity for the detector. The filter wheels can accommodate eight filters. The Generation III electronics from Astronomical Research Cameras, Inc. (ARC) (San Diego, CA), are used for this project.

Figure 5 shows a packaged 1K×1K device in a custom built rigid-flex mount which provides electrical, mechanical, and thermal connection to the device. The package was designed at RIT to mount in the detector characterization systems at the CfD. Thermal contact is made through the LCC detector package via a cold finger. The flex cable is designed to allow electrical connection through a light tight fixture. The rigid-flex board mounts to the detector testing fixture and places the detector in the optical aperture of the test system.

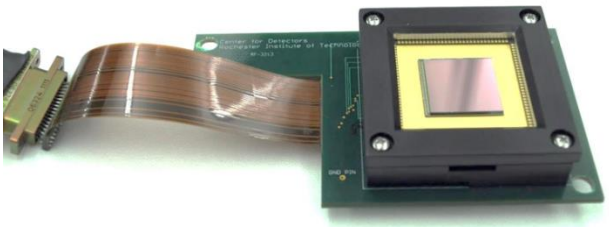

Figure 5. The photo shows a 1K×1K detector packaged in a carrier on a PCB with a flex cable, all custom-designed for this project.

Conversion gain and ROIC gain

There are a number of electrical gain stages in the signal path, and they collectively produce a net conversion gain, G_{net}, in units of e^-/ADU (Equation 1). Figure 6 shows the results of the photon transfer experiment which measures G_{net}, also called the system conversion gain. The pixel gain, G_{pixel} (e^-/V), represents the voltage change per unit charge, also expressed as the inverse of the capacitance. It is linear over small signal ranges, but becomes nonlinear when the pixel nears capacity. The detector readout has two source follower FETs between each pixel and the output pad. One is in each unit cell, and it induces a gain of G_{UC} (V/V). The other, the output FET, introduces a similar gain, referred to as G_{OUT} (V/V). The processing electronics amplify the signal, G_{AMP} (V/V). Finally, $G_{A/D}$ (V/ADU) represents the conversion between volts and analog to digital units (ADUs). G_{elec} is the convolution of these two gains as defined in Equation 2. Equation 3 defines G_{det}, which includes G_{UC} and G_{out} in the measurement. Equation 4 shows G_{MUX} is a measure of the combined output efficiency of the pixel FET and output FET in units of V/V. Measurements of G_{det} and G_{elec} are shown in Figure 6 (a).

$$G_{net} = G_{pixel} * G_{UC} * G_{out} * G_{amp} * G_{A/D} \qquad \text{Equation 1}$$

$$G_{elec} = G_{amp} * G_{A/D} \qquad \text{Equation 2}$$

$$G_{det} = G_{UC} * G_{out} \qquad \text{Equation 3}$$

$$G_{MUX} = G_{elec} \div G_{det} \qquad \text{Equation 4}$$

G_{elec} was calculated by measuring the change in ADU produced by a known change in input voltage to the ARC. Figure 6 (a) shows this relation with a calculated gain of 11.56 µV/ADU. To measure the output efficiency of the ROIC, the device is connected to the input of the electronics with the reset voltage ranging to from 0.0 to 0.5 V. This produces a perfectly linear output with a gain of 11.76 µV/ADU (Figure 6 (a)), corresponding to a ROIC output efficiency (G_{MUX}) of 98%. (Figure 6 (b)) shows the measurement of the conversion gain (G_{net}), obtained through the use of the photon transfer method, with the detector being flat field illuminated using an integrating sphere, is 4.05 e^-/ADU. The transimpedance was calculated to be 2.9 µV/e^- at 1 V reverse bias.

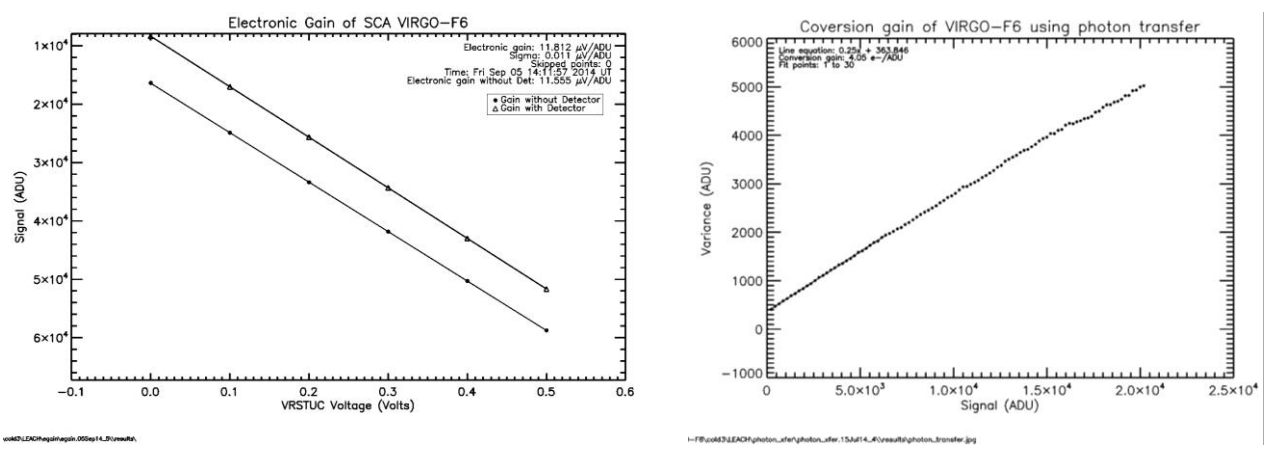

(a) (b)

Figure 6. These plots show the electronic gain (a) and the conversion gain (b) of the F6 device. The ROIC output has a gain of 11.76 µV/ADU corresponding to an output efficiency of 98% (a). The conversion gain of the F6 is 4.05 e^-/ADU (b). The transimpedance of F6 is 2.92 µV/e^-.

Table 3 summarizes the gains measured for the ARC electronics and the "F" devices. The two detectors tested from the second fabrication run gave similar results. The gain of the ARC is tunable and has been selected to have the resolution of a few e^-/ADU based on the designed pixel capacitance. The pixel capacitance of 55 fF was measured, this agrees with the expected capacitance based in the detector design. The ROIC output efficiency measurement shows the pixel FET and output FET provide minimal signal degradation.

Table 3. Table of system and detector gains and unit cell capacitance. A measurement of the ROIC output efficiency yielded ~98 %. The unit cell capacitance was measured to be 55 fF.

Detector	G_{Amp} V/V	G_{elec} µV/ADU	G_{det} µV/ADU	G_{MUX} V/V	G_{net} e^-/ADU	1/ G_{pixel} µV/e^-	C_{cell} fF
VIRGO-Fx	6.5	11.56	11.81	0.98	4.05	2.92	54.86

Full Well and Linearity

Figure 7 shows the results of the full-well and linearity experiment in which the detector is read as it is illuminated up to the full well capacity at a flux sufficient to obtain many up-the-ramp (UTR) samples. The linearity is measured by dividing the signal integrated between successive UTR samples to the initial UTR samples. An ideal linear response would give a ratio of 1.0. To measure the full well of the detector the ARC gain is reduced such that the full well of the device is less than the input referred range of the ADC. Figure 7 shows the full well and linearity measurements. The top plot shows a histogram of the full well saturation of each pixel. The median full well capacity was measured at ~420,000 e^- for an applied reverse bias of 1 V. The linearity plot on the bottom shows a well-behaved relationship between the integrated charge and count rate. A second order polynomial fit can be used to correct for the deviation from an ideal linear response (the straight line on the bottom plot in Figure 7).

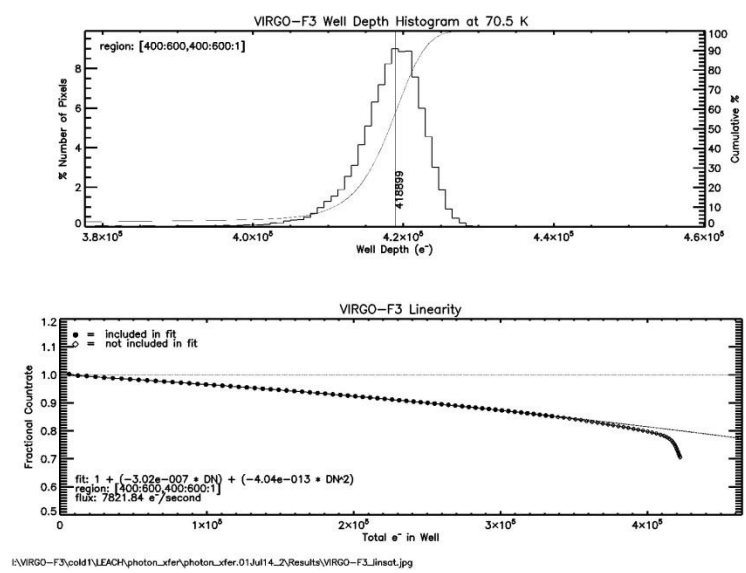

Figure 7. These plots show the full well capacity of F3. In general, all the parts tested in have a few hundred thousand electrons of full well capacity. The linearity of the device is well behaved and fit well by a second order polynomial.

Read Noise

Figure 8 shows the read noise for 14. Correlated Double Sample (CDS) read noise is about 18 e^-, while Fowler-16 pairs yields 5~6 e^-. This reduction in noise vs. fowler number matches the expected reduction which is plotted as the $1/\sqrt{n}$ reduction from the CDS noise. Although 14 is a previously fabricated MCT/Si device, it does demonstrate the promise of the MCT/Si technology as 14 already almost meets the SATIN project goal of 5 e^- read noise for Fowler-16. Future VIRGO detectors would merely have to replicate or slightly improve the performance of the existing technology to meet the SATIN project goal for the read noise.

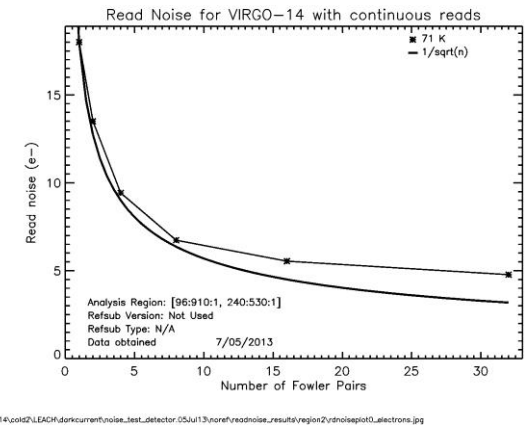

Figure 8. The read noise vs. fowler number for 14 is shown. The CDS noise is about 18 e^- and reduces to 5~6 e^- at Fowler-16. It is consistent with the expected reduction in noise vs fowler pair.

Dark Current

Figure 9 shows a comparison of the dark current behavior as a function of temperature between 14 and F3. 14 has a distinct "knee" at 100 K, below which the rise in dark current is very slow, 0.0005 e^-/second/K and above which the rise is very steep, 30 fold increase every ~15 K. F3 has a much less distinguishable knee. F3 has about an order of magnitude higher dark current, than 14 starting at ~80 K. The encouraging part is that F3 does, however, perform on par or better below 60 K.

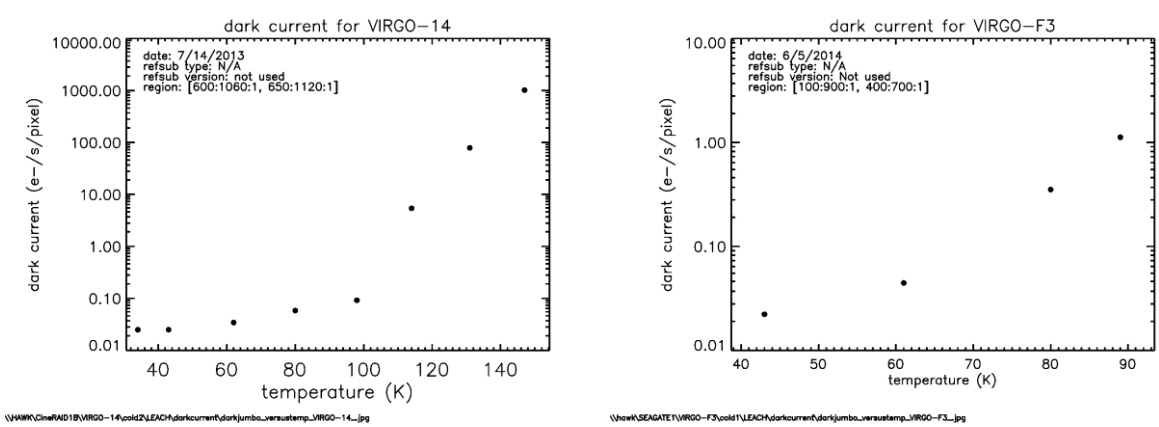

(a) (b)

Figure 9. These plots show the dark current as a function of temperature for the heritage device, 14 (a), and the new device, F3 (b).

Figure 10 shows the contrast in dark current histograms for 14 and F3. For many of the pixels, the performance is similar, the peaks being 0.03 e^-/pixel/s and 0.02 e^-/pixel/s, respectively. Where they differ is at the high end of the tail where 14 has a symmetric distribution. F3, on the other hand, has a significant tail at the high end with 25% of the pixels having dark current above 0.2 e^-/pixel/s. What is encouraging is that, except for the tail end of F3 pixels, the performance of F3 is on par with 14. Figure 10 (c) shows that the spatial distribution of the high dark current pixels in F3 is random. The extended dark current tail in F3 is believed to be due to an insufficiently thick MBE buffer layer, as will be discussed in the next section.

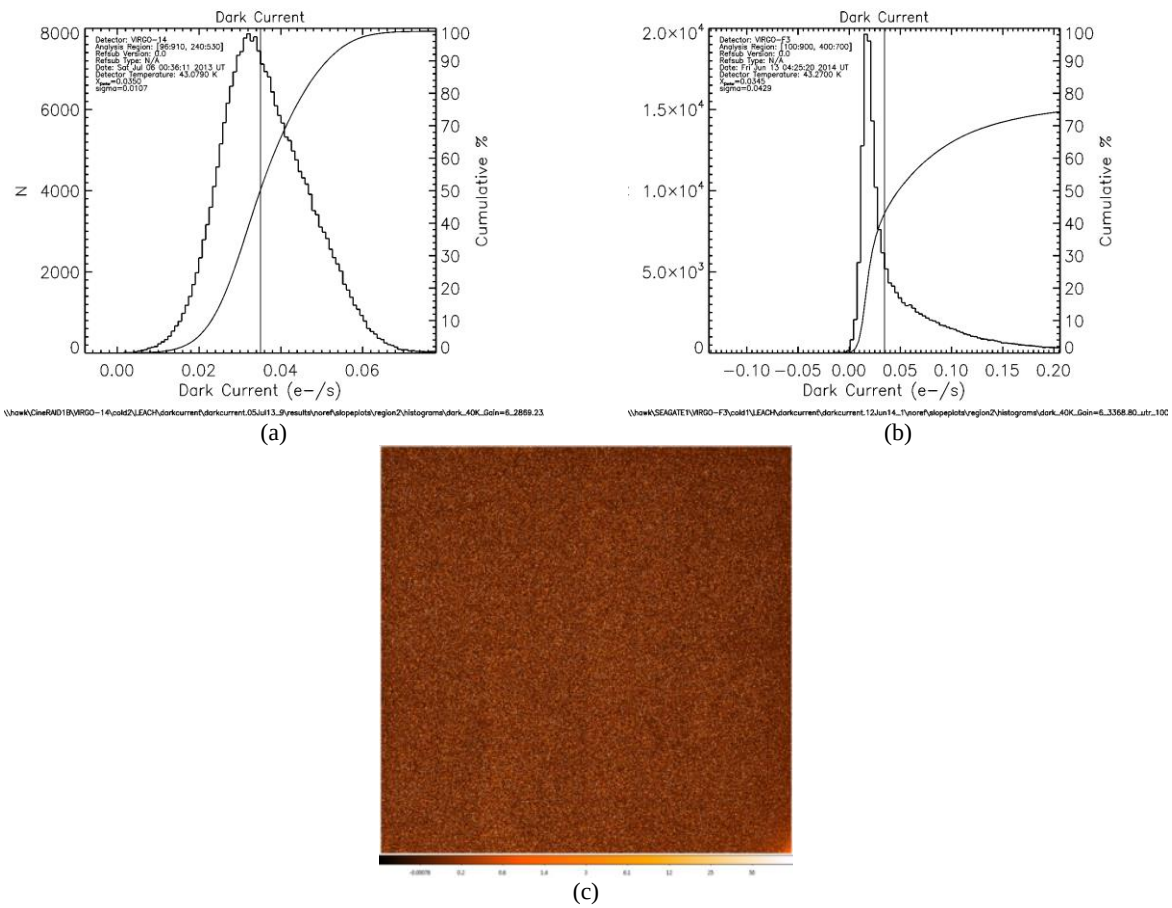

Figure 10. Dark current histograms for 14 (a) and F3 (b). The distribution of the high dark current pixels for the latter is random (c). The dark current at the peak of the distributions is actually less for F3, being 0.02 e^-/pixel/s, as compared to 0.03 e^-/pixel/s for 14.

Post thinning dark current was measured on VTHIN1. This detector is from the same wafer as F6 and was assumed to have similar dark current prior to thinning. The post thinning dark current measurement gives an indication of how the thinning process will impact dark current. Figure 11 shows that compared to F6 parts the dark current is comparable at low temperatures. The dark current of the thinned device shows a stronger dependence on temperature. The thinning process, as implemented, does not significantly increases the dark current at temperatures below ~70 K.

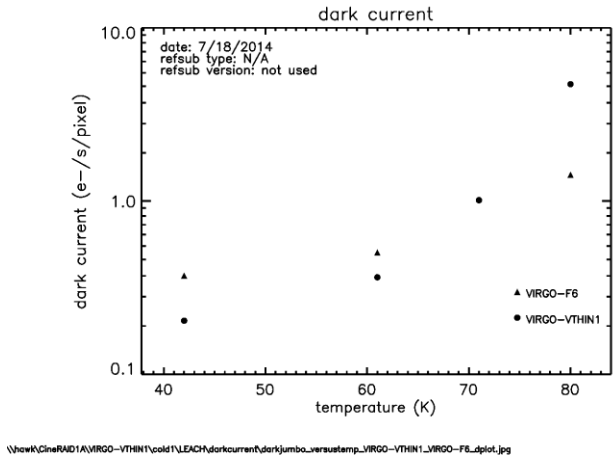

Figure 11. These plots show the dark current as a function of temperature for VIRGO-VTHIN1 to investigate the impact of the thinning process on dark current. The dark current is comparable to F6 at temperatures below ~70 K

Quantum Efficiency

The quantum efficiency (QE) experiment was performed using the diode replacement method. The detector was flood illuminated with a flat field monochromatic light source using an integrating sphere and a monochromator. The QE was then measured by placing an absolutely calibrated photodiode at the same location as the detector and taking a ratio of the detector response and the diode response.

The QE for F6 was measured and found to be ~50% (J), 75% (H), and 80% (K) as seen in Figure 12 (a). Our measurements show a long-wavelength cut-off of 2.8 µm. Because the substrate has not been removed, the short wavelength cut-off is 1.0 µm, and J-band QE is reduced by buffer absorption. The (relative) QE for VTHIN1, a device from the same wafer as F6, in which the substrate has been removed, is also shown in Figure 12 (b). It is clear that the short wavelength cutoff at 1.0 µm is absent in the thinned device. Rather, the short wavelength response extends well below 500 nm. It is important to note that the QE for the thinned device is relative and is shown to validate the substrate removal successfully removes the short-wave cut-off at 1.0 µm on F6.

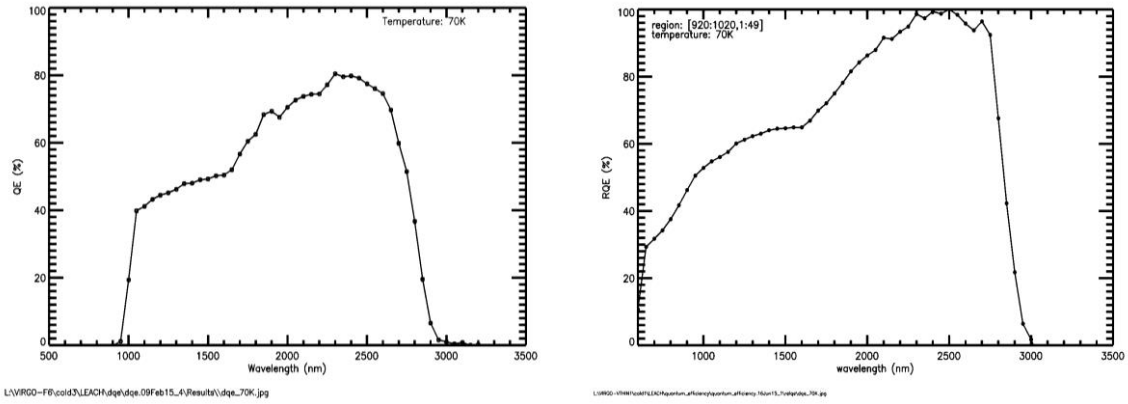

(a) (b)

Figure 12. The plots show absolute QE (±10%) for an unthinned device (F6) (a) and the relative QE for a thinned device (VTHIN1) (b). Note that the thinned part has sensitivity at wavelengths shorter than the Si cutoff at ~1 µm.

Persistence

When a detector is illuminated, the remnants of the image can persist in the device and contaminate subsequent exposures long after the original illumination. To measure persistence, the baseline dark current is measured, first, after allowing the device to settle for a long time without external stimulus. This allows any persistence images from previous illuminations to dissipate. The detector is then illuminated by a flat field light source with the wavelength at 1.6 µm. Immediately after illumination, long dark exposures are taken to measure the post-illumination dark current. The pre-illumination dark current is subtracted from the post-illumination dark current measurements, taken with the exact same exposure cadence. Any elevated dark current post-illumination will appear in the difference. Figure 13 shows such measurements for F6. The detector was illuminated to fluences equivalent to 20% (a) and 150% (b) of the device full well. The persistence at the 20% fluence is low at 0.3%, whereas the persistence at 150% fluence is at 3%. In both cases, most of the persistence is released within the first 1000 seconds after illumination.

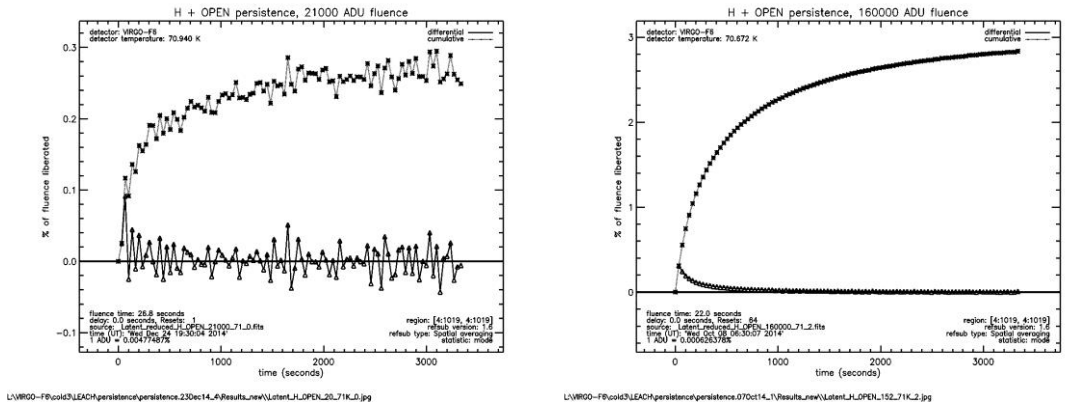

(a) (b)

Figure 13. The plots show persistence of VIRGO-F6 after being flat-field illuminated to 20% (a) and 150% (b) fluence levels.

Compared to the persistence of the 9A, the HgCdTe/CZT detector, the persistence of the F6 is larger by one to two orders of magnitude (see Figure 14) for the lower and higher fluences respectively. 9A has persistence almost an order of magnitude less than the lowest persistence measured on F6.

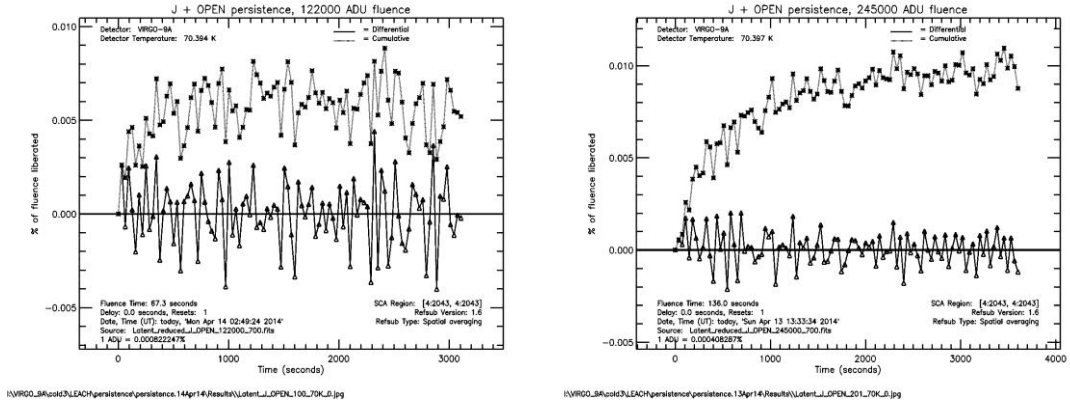

(a) (b)

Figure 14. The plots show persistence of VIRGO-9A after being illuminated to 100% (a) and 200% (b) fluence levels. The persistence of 9A, a HgCdTe/CZT detector, is up to two orders of magnitude smaller than persistence of the HgCdTe/Si detectors.

The difference in persistence of F6 between the 20% and the 150% fluences is actually a manifestation of a phenomenon in which a discrete jump in persistence occurs when the fluence level crosses 100% of the detector full well. This discrete jump as seen in Figure 15, was not seen previously (Bezawada, 2005), additional work by RVS on another program to understand process dependencies on image persistence has provided preliminary results indicating improved performance, similar to 9A, can be obtained with a process change.

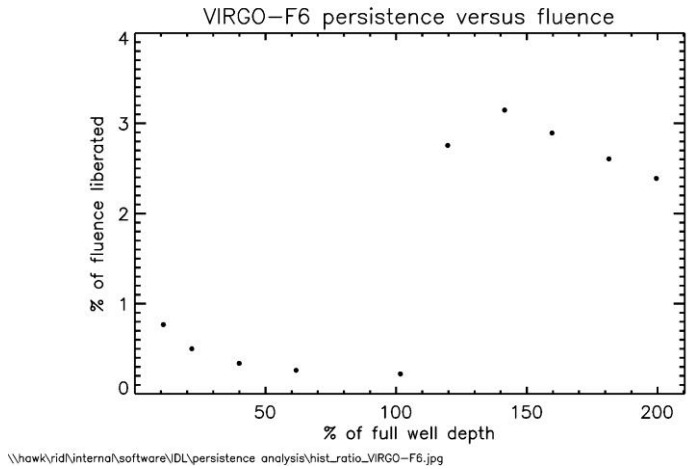

Figure 15. Plot shows the persistence vs. fluence level. As shown in the plot the persistence has a discrete increase at ~100% full well. The persistence increases from ~0.3% to ~2.8% when the illumination fluence goes above 100% of the detector full well.

Crosstalk

Crosstalk measures the amount of inter-pixel induced signal a detector exhibits. The Crosstalk for F3 was measured using the cosmic ray secondary method. With this method, long dark exposures are taken sufficient to leave the detector susceptible to enough cosmic ray secondary hits to be statistically relevant. Reduction code then rejects any events that are not normally incident on the detector nor centrally located within a pixel. The remaining events are then aggregated, dark current subtracted, and the signals in the nearest neighbors are compared to the central "hit" pixel. The results are reported as fractional percentages of the central signal. Any signal measured above the noise is due to induced signal from the central "hit". This method gave a nearest neighbor crosstalk of ~0.6% as shown in Figure 16.

detector temperature (K): 40.0
number of images: 10
number of events: 136
date: Mon Jul 21, 2014
region: [4:1019,4:1019]
crosstalk results (%):

0.05	0.59	0.03
0.56	100.00	0.56
0.08	0.43	0.05

Figure 16. Crosstalk of the nearest neighbor using the cosmic ray secondary method. The nearest neighbor crosstalk is ~0.6 %.

Intra-pixel Sensitivity

Intra-pixel sensitivity measures the variations in sensitivity to photons within a single pixel. To map out intra-pixel sensitivity, a raster scan was performed using a spot projector mounted on a three-dimensional scanning mount. The spot projector was used to scan a 3x3 pixel region at 2 µm spacing in which an exposure is taken with the beam at each location. The beam used in the measurement has a wavelength of 1.1 µm with a spot profile of 7 µm (FWHM). Intra-pixel sensitivity measurements were conducted on 9A, as the long wave cutoff of F6 and F3 allows for a significant background signal. The difference in the pixel structure between 9A and F6 is minimal and a significant difference in performance is not expected.

When the response of the 3×3 pixels for each location of the beam is overlaid on the same plot, there are nine distinct contours 20 µm apart, as expected (see Figure 17 (a)). The 50th percentile contours overlap at the borders between nearest neighbors, indicating that when the beam is straddling the border between two pixels, a photon from the beam is equally likely to be detected by either pixel. Even when the beam is centered over a pixel, there is a finite probability of a photon being detected by a neighboring pixel. As seen in Figure 16 the crosstalk between the pixels is low. The extended sensitivity of a pixel well beyond the borders and soft transition in sensitivity between neighboring pixels are likely due to the finite spot size of the beam. Lateral charge diffusion prior to charge collection could be contributing to this result as well.. The raster scan does reveal, however, that the pixel structure is symmetric in x and y directions. When the pixel responses are summed over the entire raster scanned region the summed responses are uniform across the entire region (Figure 17 (b)), proving that there are no dead regions within the pixels.

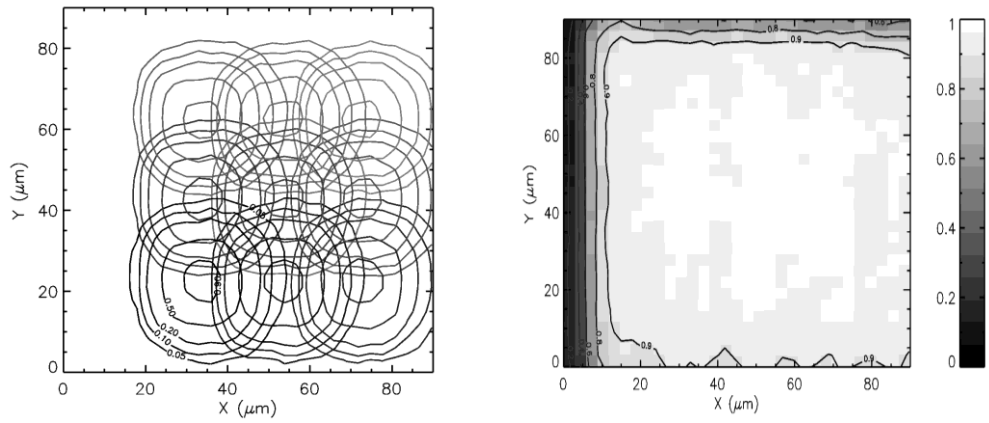

(a) (b)

Figure 17. These plots show the intrapixel sensitivity of the 9A. A raster scan with 2 µm spacing was done on a region covering 3x3 pixels using a circular beam (7 µm FWHM). The contour plots show the responses of the nine pixels overlaid on the same plot (a). The signal from each pixel is summed at each location of the beam and plotted, showing the summed response is uniform throughout the entire 3x3 pixel region (b).

4. TRANSMISSION ELECTRON MICROSCOPY OF MBE HGCDTE GROWTH ON SI

As discussed in the previous section, these detectors exhibited relatively high dark current. It was hypothesized that this may be due to: high defect density stemming from lattice dislocations in the detector material. This could be caused by insufficient buffering with the intermediate layers between the Si substrate and the HgCdTe detector material. In order to test this hypothesis, imaging of the lattice structure was required. Imaging of the buffer and detector material layers is best done with high-resolution transmission electron microscopy (TEM). TEM imaging can resolve individual lattice sites to detect lattice dislocations and defects.

Witness parts from the same lot that produced the "F" detectors were prepared and TEM imaging was performed at Cornell University's Center for Material Research (CCMR). Cross-sectional images of the parts through epitaxial layers, including buffer layers, (see Figure 18) were obtained. The figure shows how lattice defects are minimized, by use of the buffer layers, before propagating through to the HgCdTe (off to the right of the figure).

Figure 18 show the buffer layers exhibited a high concentration of lattice mismatch and defects, which is expected as these layers absorb stress from the epitaxial layers. The defects are also visible well into the second buffer layer. Higher resolution imaging of the interface between the buffer layers and the HgCdTe layer will be obtained in order to quantitatively describe the epitaxial material quality in the HgCdTe absorber. The data strongly suggests a significant concentration of defects is present in the HgCdTe layer.

In order to mitigate this problem in future process designs, the buffer layers should be made thicker to more fully absorb the stress of the mismatched epitaxial layers. This will result in less stress on the device layer and fewer dislocations and defects. In turn, this lower defect density should lead to decreased dark current.

The tail observed on F3 and F6 indicates that the thin buffer is inadequate for SWIR HgCdTe (which has a higher Cd fraction than more commonly grown MWIR HgCdTe). The benchmark MCT/Si detector, 14, was designed with thicker buffer layers and the dark current tail is absent (Figure 10).

While thick buffers significantly reduce the dark current tail, they would cause detector damage if not removed before cryogenic testing. However, substrate removal process allows selective etch removal of these buffers, and the visible/NIR-band response specs for this project already require it.

5. CONTINUING DEVELOPMENT

The initial project to develop the devices described in this paper is drawing to a close and a new phase of the project is beginning. Good progress was made in Phase I, but the final designs do not satisfy science grade requirements. The performance can meet requirements with a manageable improvement in the dark current and minor design change. In Phase II, improvements to the performance will be made to develop final devices and designs that will be ready for implementation in a 4K×4K format. The most important area to improve in Phase II is the relatively large distribution of pixels with high dark current. While the median dark current may be acceptable for some applications, it is clear that the performance would not be suitable for most astronomy applications and certainly not for low-background applications, e.g., for spectroscopy or in space. This problem is expected to be a relatively straight-forward fix using an iterative design-build-test approach.

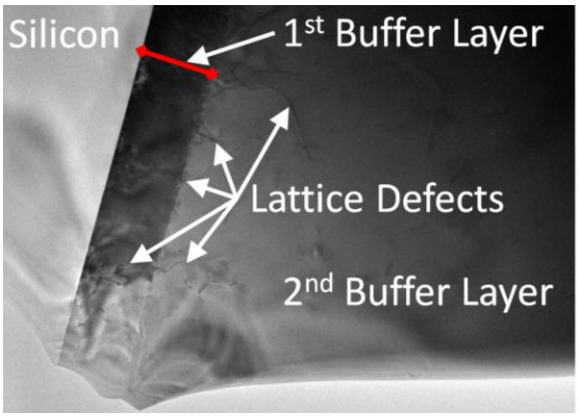

Figure 18. High resolution TEM image of a die sample. Shown are two buffer layers and the Si substrate. Lattice defects can be seen in higher density in the first layer and diminishing in the second buffer layer.

The high dark current tail and high persistence after full-well fluence, seen in some devices are likely due to the relatively thin buffer layer and a processing issue respectively. Both are being addressed by redesigning the buffer layer to be thicker and then by thinning the devices in order to achieve high quantum efficiency at shorter wavelengths. This new design combines properties from the design of the heritage device and the devices developed earlier in this project.

6. CONCLUSIONS

The MCT/Si technology is close to meeting the SATIN project goals. The dark current is as low as 0.04 e^-/sec/pixel at 60 K. The SATIN goal of 0.05 e^-/sec/pixel is specified at 80 K, at which the best measurements are ~0.10 e^-/sec/pixel (Figure 9). The CDS read noise of 18 e^-, or equivalently 5~6 e^- for Fowler-16, previously demonstrated by VIRGO-14 is on the cusp of meeting the SATIN goal. Except for the depressed QE in the J band, the QE meets the SATIN goal of 70% minimum. Persistence below 100% fluence levels is about 0.1%. If the persistence above the 100% fluence level can be reduced to this level of performance, then that would meet the SATIN goal. Note that the SATIN goal is 0.1% after 100% fluence. It doesn't actually specify over 100% fluence. The devices already meet the goal as strictly interpreted. Crosstalk is small at 0.6% and the well depth is rather large, in excess of 400,000 e^-.

7. ACKNOWLEDGEMENTS

This material is based upon work supported by the National Aeronautics and Space Administration under Grant No. NNX13AH70G issued through the APRA Program and by the National Science Foundation under Award 1207827 through the ATI Program. The TEM analysis made use of the Cornell Center for Materials Research Shared Facilities which are supported through the NSF MRSEC program (DMR-1120296).

8. REFERENCES

[1] Bangs, J., Langell, M., Reddy, M., Melkonian, L., Johnson, S., Elizondo, L., et al. (2011, April 25). Large format high-operability SWIR and MWIR focal plane array performance and capabilities. *Proc. of SPIE Infrared Technology and Applications XXXVII, 8012*, 1-12.

[2] Bezawada, N. a. (2005). Performance Overview of VISTA IR Detectors. *Scientific Detectors Workshop.*

[3] Figer, D. F., Rauscher, B., Regan, M., Morse, E., Balleza, J., Bergeron, L., et al. (2003, August 3). Independent Testing of JWST Detector Prototypes. *Proc. of SPIE Focal Plan Arrays for Space Telescopes, 5167*, 270-301.

[4] Figer, D., Agronin, M., Balleza, J., Barkhouser, R., Bergeron, L., Greene, G., et al. (2002, December). The Independent Detector Testing Laboratory and the NGST Detector Program. *Bulletin of the American Astronomical Society, 34*, 1316.

[5] Gulbransen, D. J., Black, S. H., Childs, A. C., Fletcher, C. L., Johnson, S. M., Radford, W. A., et al. (2004, April 12). Wide FOV FPAs for a Shipboard Distributed Aperture System. *Proc. of SPIE Infrared Technology and Applications XXX, 5406*, 305-316.

[6] Hanold, B., Figer, D., Lee, J., Corrales, E., Mears, L., Bangs, J., et al. (2013). Characterization of a Large Format HgCdTe on Si Focal Plane Array. *Proc. of The Scientific Detector Workshop*.

[7] Jóźwikowski, K., Jóźwikowska, A., Kopytko, M., Rogalski, A., & Jaroszewicz, L. R. (2012). Simplified model of dislocations as a SRH recombination channel in the HgCdTe heterostructures. *Infrared Physics and Technology, 55*(1), 98-107.

[8] Melkonian, L., Bangs, J., Elizondo, L., Ramey, R., & Guerrero, E. (2010, April 5). Performance of MWIR and SWIR HgCdTe-based focal plane arrays at high operating temperatures. *Proc. of SPIE Infrared Technology and Applications XXXVI, 7660*, 1-11.

[9] Puschell, J. (2009, March). Quantum Limited Imaging Detectors for Earth System Science Applications. *Quantum-Limited Imaging Detectors Workshop*.

[10] Reddy, M., Peterson, J. M., Vang, T., Franklin, J. A., Vilela, M. F., Olsson, K., et al. (2011). Molecular Beam Epitaxy Growth of HgCdTe on Large-Area Si and CdZnTe Substrates. *Journal of Electronic Materials, 40*(8), 1706-1716.

[11] Simms, L., Figer, D., Hanold, B., Kerr, D., Gilmore, D., Kahn, S., et al. (2007, August 26). First use of a HyViSI H4RG for astronomical observations. *Proc. of SPIE Focal Plane Arrays for Space Telescopes III, 6690*, 1-33.

[12] Svitak, A. (2013, July 22). *Technical, Cost Issues Persist for Webb Telescope*. Retrieved June 24, 2015, from Aviation Week Network: http://aviationweek.com/awin/technical-cost-issues-persist-webb-telescope